RSC Applied Polymers

PAPER

View Article Online
View Journal

Cite this: DOI: 10.1039/d6lp00041j

Engineering deuterated bacterial cellulose *via* biosynthesis for neutron applications

Amanda Muñoz-Juan,†[a] Daniela Diaz,[a] Judith Marin-Ortega,[a] Nerea Murugarren,‡[a] Mariano Campoy-Quiles,[a] Felipe Zamorano,[b] Consuelo Guardiola,[b] Martín Pérez §[b,c] and Anna Laromaine *[a]

Received 3rd February 2026,
Accepted 3rd May 2026

DOI: 10.1039/d6lp00041j

rsc.li/rscapplpolym

Deuterated bacterial nanocellulose (dBNC) combines the biocompatibility and versatility of cellulose with the distinctive properties of deuterium, thereby facilitating the development of functional materials and their potential future applications in neutron science. We applied a scalable film-to-film biosynthesis protocol that reduces costs and time while achieving controlled deuterium incorporation into the biosynthesis of bacterial nanocellulose (BNC) using *Komagataeibacter xylinus*, adapted to D_2O and deuterated glycerol. Spectroscopic analyses (FTIR, Raman, NIR, SR-μFTIR) confirmed the presence and homogeneous distribution of O–D and C–D bonds in the membrane. At the same time, physical properties, such as crystallinity and surface charge, remained comparable to those of native BNC. Neutron irradiation experiments demonstrated that dBNC films interact with fast neutrons, producing recoil deuterons, which supports their potential as biofriendly materials of interest for neutron science. This study paves the way for future use of dBNC as a promising material in neutron-based technologies and confirms the applicability of the optimized approach for its production and characterization.

Introduction

The pursuit of biocompatible materials is gaining momentum across various disciplines, with cellulose emerging as a particularly prominent material due to its natural abundance and properties, including biocompatibility, biodegradability, and the ability to be readily functionalized *via* its numerous hydroxyl groups.[1] This biopolymer is being extensively investigated for applications in biomedicine, electronics, materials science, and food science.[2–6] Furthermore, its deuterated variants are also being examined, enlarging the applications of this material.[7–11] Initially, deuterated cellulose was used in fundamental research to elucidate cellulose structure and its interactions with other molecules. Following this strategy, deuterated cellulose has been used to gain insight into its interactions with biomolecules and solvents, thereby improving its use as a drug delivery system. More recently, it has been proposed as an anticounterfeiting material[10] due to its different absorption properties in the infrared and near-infrared regions.

Deuterated cellulose can be obtained through different chemical reactions, the main limitation of which is that only accessible hydrogens, those found in hydroxyl groups, are interchanged with deuterium.[10,12] For that reason, more studies have focused on producing deuterated cellulose directly by culturing plants or microorganisms with deuterium-enriched nutrients, thereby incorporating deuterium as –CD, and –OD chemical bonds in the structure of cellulose.[9,13] Bacteria are more resistant to deuterium toxicity than plants and grow faster, which speeds the production of deuterated cellulose.[14] It has been reported that the production of deuterated bacterial cellulose (dBNC) is primarily achieved using *Komagataeibacter xylinus* and *Gluconacetobacter hansenii* strains.[7,14] Some studies have opted to replace all nutrients with their deuterated counterparts completely.[9,14] Although this approach increases the deuterium concentration in the final pellicle, it also significantly increases production costs and duration. Alternatively, other studies have substituted H_2O with D_2O and employed a deuterated carbon source, such as deuterated glucose or glycerol.[7,11,15] In all cases, bacteria are

[a]*Institut de Ciència de Materials de Barcelona, ICMAB-CSIC, Bellaterra 08193, Spain. E-mail: alaromaine@icmab.es*
[b]*Institute of Microelectronics of Barcelona, IMB-CNM (CSIC), Bellaterra 08193, Barcelona, Spain*
[c]*Consejo Nacional de Investigaciones Científicas y Técnicas (CONICET), Buenos Aires, Argentina*
†Current position: Danish Research Institute of Translational Neuroscience - DANDRITE, Nordic-EMBL Partnership for Molecular Medicine. Aarhus University, Department of Molecular Biology and Genetics, 8000 Aarhus, Denmark.
‡Current position: Centro de Biología Molecular Severo Ochoa, CSIC-UAM, Nicolás Cabrera 1, Cantoblanco, 28049, Madrid, Spain.
§Current position: Comisión Nacional de Energía Atómica (CNEA), Av. Bustillo 9500, San Carlos de Bariloche, Río Negro, Argentina, and Instituto Balseiro, Universidad Nacional de Cuyo, Argentina.

acclimated to deuterated media by gradually increasing the concentration of deuterated compounds. The bacteria cultivated at each stage are subsequently used to inoculate the next medium with a higher deuterium concentration, typically *via* a 1 : 5 dilution and 50 ml volumes.[9] Deuterium atoms form bonds that exhibit different vibrational frequencies, stability, and reactivity from hydrogen bonds.[16] Therefore, dBNC has been used to understand polymer structure, biosynthesis, and to visualize biomacromolecules' absorption.[8,11,13,17]

Additionally, the potential of deuterated polymers in areas such as active-layer materials for clean energy, future electronics, and neutron science is emerging.[14,18–20] Among them, neutron moderators are materials used in neutron imaging or therapy that interact with neutrons, slowing fast neutrons (>1 MeV) and promoting recoil, while ideally avoiding capture.[21] The slowed neutrons are used in various neutron-based techniques, including neutron imaging, small-angle neutron scattering (SANS), and neutron diffractometry.[22,23] Neutron moderator materials contain small atoms with a high scattering cross-section. Therefore, H_2O is widely used as a moderator material because hydrogen has the smallest atomic size. Other moderators include heavy water (D_2O), sodium, and graphite.[24] These materials have limitations depending on the application, such as a high reduction signal due to material self-absorption and limited tunability. One of the optimization strategies is to substitute hydrogen atoms with deuterium, which has a lower thermal neutron capture section (5.5×10^{-4} b *vs.* 0.33 b for hydrogen),[25,26] which translates to a 600-fold reduction in self-absorption.[27–32] Consequently, deuterated bacterial cellulose could be produced with different degrees of deuteration and final shapes, providing design flexibility in comparison with current materials used as moderators.[25–27]

In this study, we applied a protocol that minimizes the cost and time required to produce bacterial nanocellulose (BNC), named "film to film".[33] We evaluated whether it could be used to produce different degrees of deuterated bacterial nanocellulose (dBNC). Posteriorly, dBNC films were fully characterized, including the final and intermediate membranes, with special interest in techniques such as FT-IR, NIR, and Raman spectroscopy to quickly and non-destructively confirm the presence of deuterium. Finally, we evaluate the interaction of dBNC films with neutrons. Consequently, this paper aims to present and discuss experimental observations of deuterated cellulose, focusing on H/D effects and distribution, and to encourage further practical applications of deuterated polymers.

Results and discussion

Deuterium incorporation into BNC films during the adaptation process

The cellulose produced by bacteria, known as bacterial nanocellulose (BNC), can be made by different bacterial strains and carbon sources (Fig. 1A).[15,34,35] The production of BNC is hindered by the biosynthesis process, which can take time and incur reagent costs, especially for deuterated cellulose. Deuterated glycerol (D-gly) is usually preferred over deuterated glucose[9,11,17] because its metabolism acidifies the media less, increasing cellulose yield, and it is cheaper than deuterated glucose.[14,36] To avoid the toxic effects of deuterium on bacteria while producing deuterated bacterial nanocellulose, *K. xylinus* is gradually acclimated to deuterium by culturing the bacteria in media with low deuterium levels and transferring those adapted to a medium with a higher deuterium concentration. To reduce production time and costs, we used the "film-to-film" technique applied for BNC.[33] This technique involves placing freshly harvested BNC films rich in bacteria into fresh media, allowing the growth of a new membrane at the air-media interface (Fig. 1B).[33] The production time depends on the bacteria concentration, the culture media volume, and the bacteria's acclimatization. The film-to-film technique offers two main advantages: the presence of adapted bacteria already in the film formed at the interface and the lower media volumes required, resulting in faster production time. In our hands, we adapted the bacteria into 2 ml of medium, and it took 7–10 days to harvest a new film from the culture surface.

Using the film-to-film protocol, H_2O was gradually replaced by deuterium oxide (D_2O) in 25% increments until the medium reached 100% D_2O. Films formed in this medium displayed the ν(O–D) at 2480 cm^{-1}, not present in natural BNC films (Fig. 2A-i, ii). The ν(O–H) at 3340 cm^{-1} was also observed in dBNC, indicating that OD bonds did not fully replace hydroxyl groups.[11] To compare trends in deuterium incorporation across different growth conditions, we calculated the

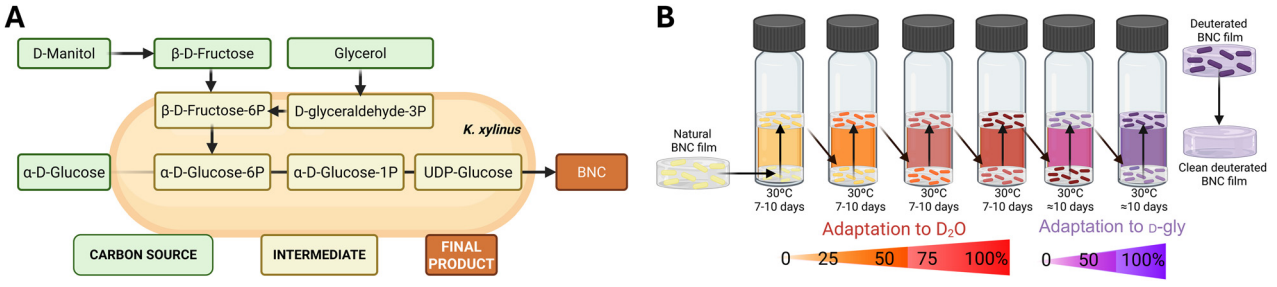

Fig. 1 Synthesis of deuterated bacterial nanocellulose (dBNC). (A) Different carbon sources can be used to produce dBNC. (B) Deuteration process through the film-to-film protocol.

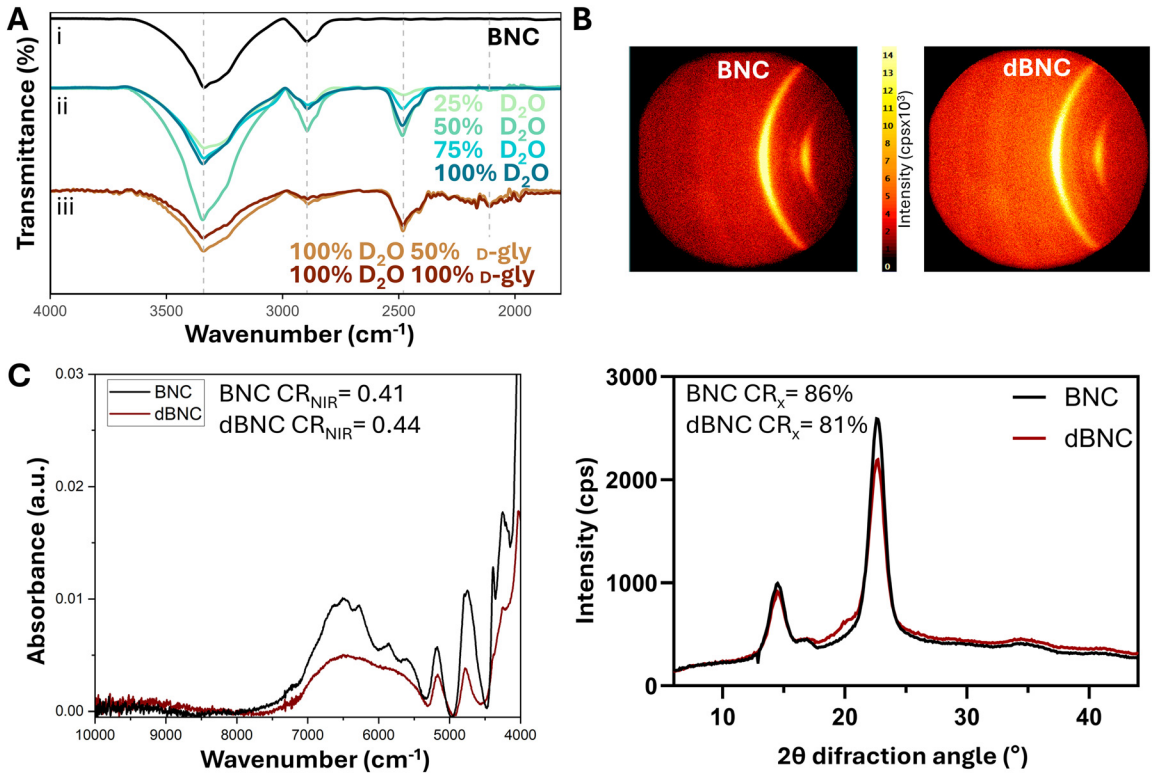

Fig. 2 Chemical composition and crystallinity of dBNC films. (A) FT-IR characterization of the films at different stages. (i) Natural BNC film. (ii) Films produced after adaptation to D_2O: 25%, 50%, 75%, and 100% D_2O. (iii) Films produced after adaptation to D-gly: 100%D_2O + 50% D-gly and 100% D_2O + 100% D-gly. (B) GADDS images (2D diffraction pattern) from natural and deuterated BNC films and their 1D diffraction pattern plots of 2θ *versus* intensity. The crystallinity index from X-ray data (CR_X) for each sample is represented in the graph. (C) NIR spectra of natural and deuterated BNC. The crystallinity index from NIR measurements (CR_{NIR}) for each sample is present in the graph.

ratio between the maximum absorption of OD (2480 cm^{-1}) and OH (3340 cm^{-1}) peaks to be interpreted as semi-quantitative indicators of relative deuterium incorporation levels. During the adaptation process, we observed that increasing D_2O, we augmented the ratio (OD/OH) from 0.11 ± 0.05 (25% D_2O growth media) to 0.48 ± 0.08 when cultured with medium with 100% D_2O (Table 1).

Once bacteria adapted to grow in D_2O, we introduced deuterated glycerol (D-gly) into the media in two steps, increasing its concentration by 50%. In both steps, we observed the O–D bond at 2480 cm^{-1} and the carbon–deuterium (C–D) bond at 2110 cm^{-1} (Fig. 2A-iii), which confirmed the incorporation of deuterium in the film.[11] The ratio CD/CH was 1.27 ± 0.80 in dBNC films grown in medium with 50% D-gly and 100% D_2O, indicating that nearly every C–H bond has a corresponding C–D bond. When D-gly was the main carbon source in the media (100% D-gly + 100% D_2O), the ratio CD/CH increased to 2.32 ± 0.70, showing a rise in C–D bonds compared with C–H bonds. The presence of C–H and O–H bonds in deuterated films is expected, since there are still compounds in the media (*e.g.*, peptone, citric acid, yeast extract) that contain hydrogen. A full substitution of C–H and O–H bonds by their deuterium counterparts is possible when all reagents are deuterated, but the cost of production also increases steadily.[9,14]

Physical properties of dBNC films

The incorporation of deuterium in BNC films could produce changes in cellulose's crystallinity. Cellulose is a polycrystalline structure with crystalline and amorphous regions, which was reflected in the general area detector diffraction system

Table 1 Ratios between natural and deuterated bonds in BNC films at different stages of adaptation. Values represent mean ± SD (standard deviation

	Growth media					
Ratios	25% D_2O	50% D_2O	75% D_2O	100% D_2O	100% D_2O 50% D-gly	100% D_2O 100% D-gly
OD/OH A_{2480}/A_{3340}	0.11 ± 0.05	0.34 ± 0.05	0.29 ± 0.03	0.48 ± 0.08	0.65 ± 0.03	0.76 ± 0.10
CD/CH A_{2110}/A_{2895}	—	—	—	—	1.27 ± 0.80	2.32 ± 0.70

(GADDS) image of both natural and deuterated BNC (Fig. 2B). The X-ray diffraction pattern of both natural and deuterated BNC (Fig. 2B) exhibits the characteristic peaks of cellulose at 2θ = 14.5°, 16.5°, and 22.7° corresponding with planes (10), (110), and (200).[17] According to the literature, we calculated the crystallinity index (CR_X) by the Segal peak height method[17,37,38] and found that BNC and dBNC have CR_X values of 86% and 81%, respectively (Fig. 2B). Using near-infrared (NIR) spectroscopy, we also detected differences between BNC and dBNC spectra, especially in the 5500–7000 cm^{-1} region, where the O–H first overtone is present in cellulose.[39] We calculated the crystallinity index (CR_{NIR}) for BNC and dBNC following the method described by Inagaki, T. *et al.*[39] by measuring the area under the peak curves of the amorphous region peaks at 6950 cm^{-1}, and the crystalline regions at 6450 cm^{-1} and 6287 cm^{-1}. BNC and dBNC have CR_{NIR} values of 0.41 and 0.44, respectively (Fig. 2C). Although CR_X and CR_{NIR} are derived from different measurement principles and are therefore not directly comparable, a consistent correlation between them has been shown.[39] Both methods indicate that the differences between BNC and dBNC fall within the error of the technique. In accordance with previous studies,[17,39] these results indicate that BNC and dBNC present comparable levels of crystallinity within the resolution of the applied methods.

Films were blended to obtain fibers, and their surface charge was characterized by measuring the Z-potential. Natural and deuterated BNC fibers exhibit moderate stability with similar Z-potentials, −17 ± 0.7 mV and −18 ± 0.4 mV, respectively. Therefore, deuterium incorporation did not affect the surface charge or the colloidal stability of these fibers.

Distribution of O–D and C–D chemical bonds

Raman Microspectroscopy and synchrotron radiation-based Fourier-transform infrared microspectroscopy (SR-μFTIR), two complementary techniques, were employed to assess the biodistribution of C–D and O–D chemical bonds within the samples. We used Raman spectroscopy to obtain a 25 × 25 point image, where each point corresponded to a single spectrum. The average spectrum is shown in Fig. 3A. The cellulose Raman spectrum is usually divided into three regions based on the chemical fingerprints of each region. Hydrogen bond (–OH) vibrations are found above 3000 cm^{-1};[40] whereas carbon bonds are located between 1000–1600 cm^{-1}, except for the –CH vibration that is found at 2900 cm^{-1}.[41,42] The third region between 1600–2900 cm^{-1} is denominated the silent region due to the absence of absorption peaks in protonated cellulose. In this last region, two peaks appear due to the deuteration process: the O–D bond at 2500 cm^{-1} and the C–D bond between 2000–2400 cm^{-1}.[16,43]

In our case, dBNC films presented one peak at *ca.* 2100 cm^{-1}, which we assigned to the C–D bond,[43] and another peak at *ca.* 2470 cm^{-1}, assigned to O–D.[16] Unlike FTIR, Raman spectroscopy could detect a weak signal from C–D bonds in the dBNC produced with just 100% D_2O in the media. To analyze the distribution of the deuterated peaks in the sample, we performed a statistical analysis to quantify the number of pixels for each absorption intensity at each peak, obtaining histograms of intensities for O–D and C–D bonds (Fig. 3B); and we mapped the C–D and O–D peaks in a 25 × 25 point film image (Fig. 3C), observing a homogenous distribution of chemical bonds. The distribution of pixels for non-deuterated

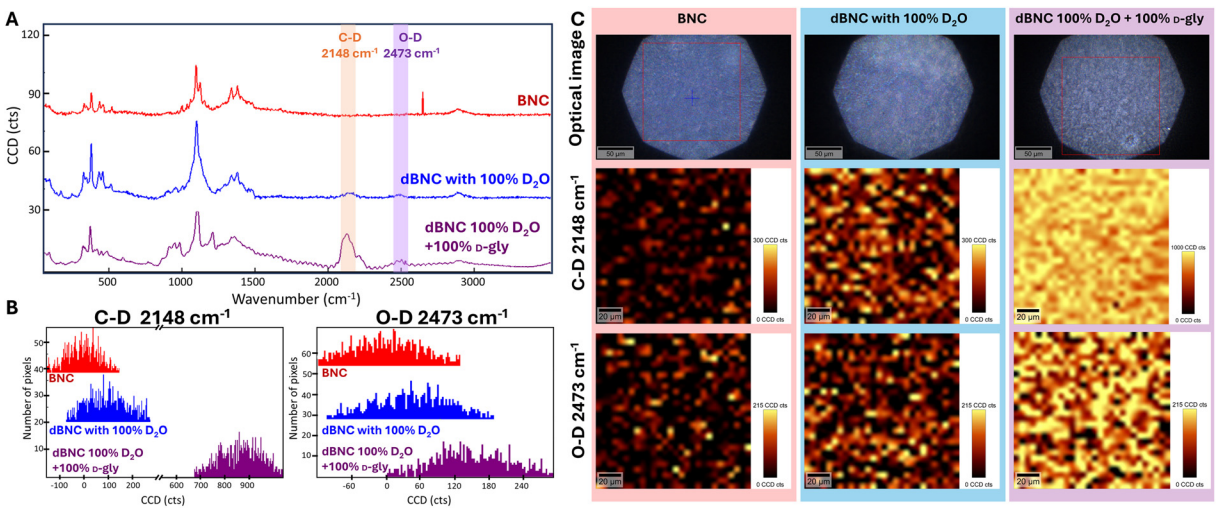

Fig. 3 Raman analysis of dBNC. (A) Raman spectra of natural BNC (red), deuterated BNC produced in medium with 100% D_2O (blue), and in medium with 100% D_2O and 100% D-gly (purple). The relevant peaks from deuteration, C–D at 2148 cm^{-1} and O–D at 2473 cm^{-1}, are highlighted in orange and purple squares. (B) Number of pixels detected for each intensity for C–D bond (left) and O–D bond (right). The same color legend is maintained. (C) Raman spectroscopy mapping of natural BNC, dBNC with 100% D_2O, dBNC with 100% D_2O + 100% D-gly. The same background and processing were kept for all images. The scale bar of the optical image is 50 μm and 20 μm for the Raman images. Color scale values range from black (low) to yellow (high). The dBNC intensity scale for 100% D_2O and 100% D-gly differs from the other samples due to the high intensity observed.

films is around zero, as expected. The incorporation of C–D and O–D bonds into the film shifts the histogram to the right, indicating a greater presence of pixels with higher absorption intensity at each deuterated peak (Fig. 3B). The average intensity of pixels at 2473 cm^{-1} (O–D bond) increased to 60 cts in films produced in 100% D_2O media and to 150 cts in films produced in media with 100% D_2O and 100% D-glycerol. The introduction of a deuterated carbon source increases the incorporation of O–D bonds, likely due to a more abundant deuterium environment. Reassuringly, the average intensity of the C–D bond increased by almost one order of magnitude when films were produced in media containing 100% D-gly, underscoring the importance of using a deuterated carbon source.

We complemented the previous spatial characterization of deuterated films by evaluating the spatial distribution of deuterated chemical bonds in deuterated fibers using SR-μFTIR analysis. The C–D and O–D peaks appeared at 2110 cm^{-1} and 2480 cm^{-1}, respectively (Fig. 4A).[11] The C–D intensity was low, preventing the acquisition of an image map. On the other hand, the O–D intensity peak enabled localization of O–D along dBNC fibers and complemented the previous Raman mapping. During sample preparation, a drop of dBNC fibers is placed on a CaF_2 window and dried overnight under vacuum. At this step, fibers can deposit onto other fibers, increasing the amount of material analyzed. Therefore, single-fiber resolution is not achieved with this technique, and a larger sample amount, a darker sample (Fig. 4B), is correlated with a greater increase in O–D intensity in the map (red-orange region in Fig. 4C).

Neutron radiation fingerprint of deuterated cellulose

Natural and dBNC membranes were irradiated at the Centro Nacional de Aceleradores (CNA) with neutrons up to 8 MeV of energy, for 45 min, and compared them to evaluate their interaction with neutrons. The 50 μm thick films were placed on top of a 3 × 3 mm silicon carbide (SiC) detector, with a 50 μm epitaxial layer, as shown in the insight of Fig. 5A.[44] The number of detected events is plotted in Fig. 5A as a function of energy for both BNC and dBNC, showing an increased number of detected counts in the range, compared to the bare detector. In the absence of a membrane, the detected signal arises from neutron interactions within the SiC active volume, primarily *via* elastic scattering with silicon and carbon nuclei. These interactions produce recoil Si and C ions; however, due to their relatively high mass, the energy transferred per collision is limited, resulting in a lower detected signal. When a membrane is placed on top of the detector, additional interaction channels are introduced through elastic scattering of neutrons with hydrogen or deuterium nuclei.

The difference between BNC and dBNC is a shoulder observed in the 1.85–2.15 MeV range, which is attributed to the deuterium contribution, indicating an even higher ionization yield than hydrogen. This data confirms the presence of deuterium in dBNC membranes and its interaction with neutrons. Considering the nature of both films and the neutron field, the experimental setup was simulated using the Particle and Heavy Ion Transport code System (PHITS) code, based on the Monte Carlo method.[45] The overall behavior observed in the simulations is consistent with the experimental trends (Fig. 5A), confirming that above 2 MeV dBNC membranes interact with neutrons, producing a higher number of counts per incident neutron than BNC membranes, indicating a stronger contribution from recoil deuterons than from recoil protons. This is consistent with the extended high-energy tail observed in spectra from the deuterated membrane.

The contribution of each particle to the total simulated spectrum of dBNC membrane is shown in Fig. 5B. Protons and deuterons are significantly lighter than silicon and carbon ions, which results in a more efficient energy transfer per collision. As expected from two-body elastic scattering kinematics, a larger fraction of the incident neutron energy can be transferred to these light nuclei. This process produces recoil protons and deuterons with relatively high kinetic energies, which in turn deposit more energy within the detector's active volume. In this configuration, the maximum energy transferred by neutrons to deuterons and protons is approximately 7.1 MeV and 8 MeV, respectively (Fig. S1). Their corresponding ranges in SiC are about 300 μm for protons and 150 μm for deuterons. This implies that both particles can traverse the entire active region of the detector. However, the linear energy

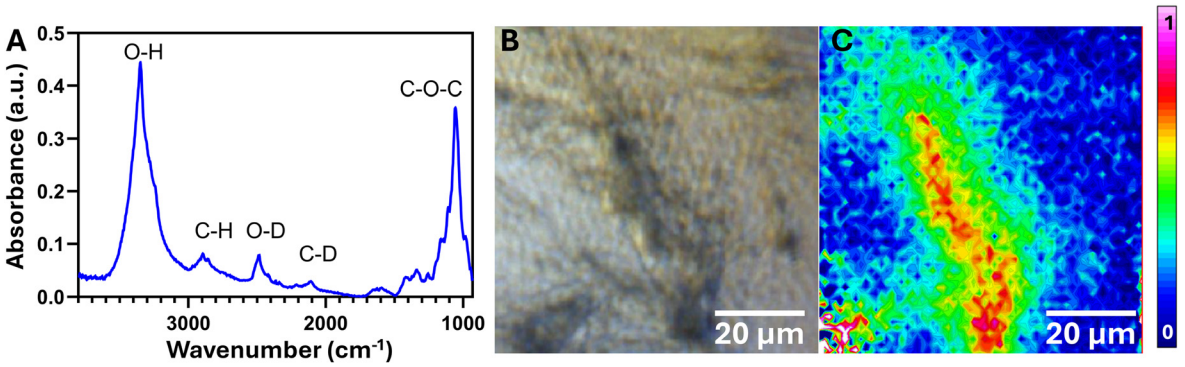

Fig. 4 SR-μFTIR characterization of dBNC. (A) Average spectra of dBNCf. Principal peaks are highlighted. (B) Optical microscope image of dBNCf and (C) integrated intensity of O–D stretching peak (2500–2460 cm^{-1}) of the same area of dBNCf imaged.

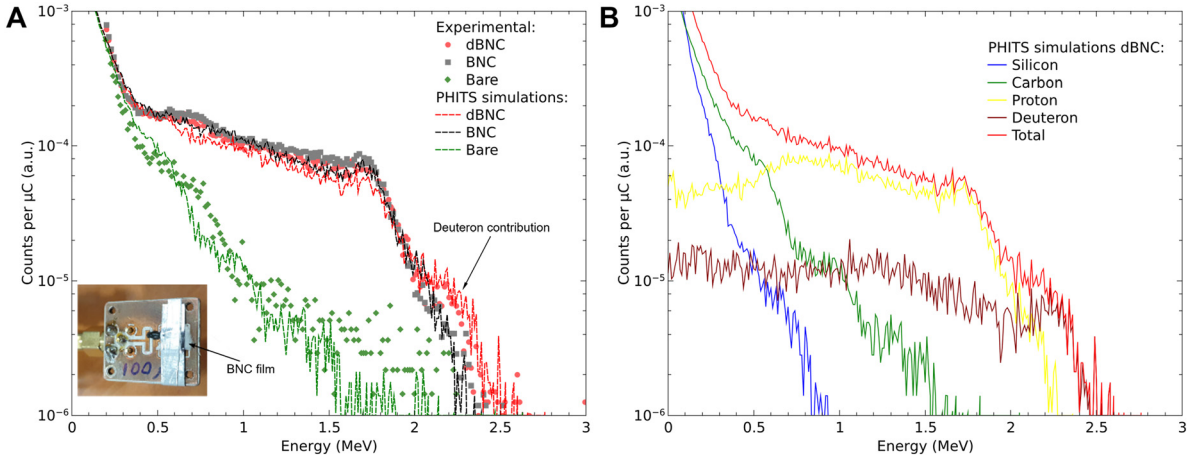

Fig. 5 Neutron radiation characterization. (A) Experimental spectra obtained in the neutron measurements and PHIT simulations for the dBNC (red), the natural BNC (black), and the bare detector (green). Markers represent experimental data; dotted lines indicate PHITS simulations. Inset: image of the SiC detector covered with a 50 μm-thick dBNC membrane. (B) Simulated contributions to the detected signal in dBNC membranes, arising from neutron elastic scattering: recoil Si (blue) and C ions (green) from the detector, and recoil protons (yellow) and deuterons (brown) from the dBNC membrane.

transfer (LET) of deuterons is higher than that of protons (Fig. S1), resulting in a greater maximum energy deposition, as observed in Fig. 5B.

Conclusion

Cellulose deuteration offers significant potential to enhance material properties and broaden functional applications. However, traditional biosynthesis methods need refinement to boost efficiency and resource utilization. The film-to-film protocol introduced here effectively addresses these challenges by reducing the volume of deuterated media and accelerating deuteration. This method not only streamlines production but also enables detailed monitoring of bacterial adaptation during intermediate stages, an aspect largely underexplored in previous studies. Comprehensive spectroscopic analyses confirmed the successful incorporation of O–D and C–D bonds, indicating a uniform distribution of deuterium within the cellulose matrix. The partial retention of O–H and C–H bonds reflects incomplete substitution in the culture media, potentially offering a tunable balance between deuterated and non-deuterated components. Deuterium incorporation did not produce detectable changes in cellulose crystallinity within the resolution of the applied techniques. The preservation of crystallinity suggests that key structural features of native cellulose are retained. The manipulation of the deuterated films was qualitatively similar to that of the non-deuterated counterparts, indicating that the films seem to have similar mechanical properties.

The neutron experiments confirmed the presence of deuterium in the membranes and the different recoil behavior with fast neutrons. The interaction between deuterium and fast neutrons opens avenues for their use in neutron-based analytical techniques, such as neutron imaging, and suggests the potential of these films for low-absorption applications as neutron-interacting material. This capability not only underscores the functional innovation enabled by the optimized biosynthesis method but also provides a basis for assessing scalability, encouraging further exploration of the practical applications of deuterated polymers, with broader implications for materials science and neutron technology.

Experimental

Materials and strains

Komagataebacter xylinus NCIMB 5346 (*K. xylinus*) was purchased from the Spanish Type Culture Collection (CECT, Spain).

Standard Hestrin-Schramn (HS) media: 20 g l^{-1} of dextrose, 5 g l^{-1} of peptone, 5 g l^{-1} of yeast extract (Conda Lab.), 6.8 g l^{-1} of sodium phosphate dodecahydrate, and 1.15 g l^{-1} of citric acid monohydrate (Merck) and MilliQ water. For the cleaning process, ethanol (Panreac) and 0.1 M NaOH (Merck) were used.

Deuterated compounds: D_2O and D-glycerol UD8-99% (Eurisotop).

Synthesis of deuterated BNC films

We followed the "Film-to-film" protocol.[33] This consists of placing freshly harvested BNC films at the bottom of the recipient with HS media. We used 24-well plates containing 2 mL of standard HS medium or HS medium supplemented with deuterated compounds. Initially, we adapted *K. xylinus* to D_2O by increasing the heavy water concentration by 25% at each step. BNC films rich in *K. xylinus* were placed at the bottom of a 24-well plate containing 2 ml of HS media with 25% D_2O. After 7–10 days, another film was formed in the air–liquid interface. Following the same procedure, the newly formed

film was used to adapt bacteria to HS media with 50% D_2O. This step was repeated until adaptation to HS media with 100% D_2O was achieved. Once bacteria were adapted to heavy water, we adapted bacteria to the deuterated carbon source, D-glycerol (D-gly). We adapted in two steps, 50% D-gly and 100% D-gly. The media for each step were sterilized using a 0.22 μm (Millex™ MP filter Sterile) filter and two 15 minute UV sterilization cycles. Bacterial cellulose films acquired the shape of wells in a 24-well plate, with a final area of approximately 1.93 cm^2.

Bacterial debris from the films was removed using a previously established protocol[33,46] to characterize the membranes further. BNC films were introduced into 1 : 1 ethanol : MilliQ water under stirring for 10 minutes, followed by 10 minutes in MilliQ water. Then, the films were subjected to two rounds of 20 minutes boiling in MilliQ water and two rounds of 20 minutes boiling in 0.1 M NaOH (Sigma). Finally, the films were transferred to MilliQ water baths to achieve a neutral pH (pH 6.5). Films were introduced in D_2O and autoclaved at 121 °C, 30 minutes. Films were placed between Teflon surfaces, pressed with one kg weight, and dried at 60 °C overnight (17 h). dBNC fibers (dBNCf) were obtained by blending 1 mg dBNC films in 100 ml MilliQ water for 30 minutes with a commercial blender. Fibers were filtered from MilliQ water and redispersed into 5 ml D_2O, yielding a final concentration of 200 μg ml^{-1}.

FT-IR

BNC and dBNC films obtained after each adaptation step were dried overnight at 60 °C and folded twice to enhance the signal from chemical bonds. Analysis was conducted using FTIR (JASCO FTIR 4700, Madrid, Spain) in transmission mode at a spectral resolution of 4 cm^{-1}; 512 scans were averaged, and the measurement range was 400–4000 cm^{-1}. The spectra were processed with Spectra Manager™ Suite software to reduce CO_2 and H_2O noise, perform baseline correction, and smooth the data. The spectrum shown is the average of three different scans. Ratios were calculated by converting transmittance values to absorbance, then dividing by the average absorbance for each chemical bond.

NIR FTIR spectra were recorded on a Bruker Vertex 70 spectrometer equipped with a DLaTGS detector and a KBr beamsplitter. The spectral resolution was 4 cm^{-1}, and 32 scans were averaged over a measurement range of 3000–9996 cm^{-1}. Baseline correction and smoothing were applied using Origin software. To estimate the crystallinity in each sample, we followed the equation (eqn 1) proposed by Inagaki *et al.*[39] The crystallinity index using NIR spectra (CR_{NIR}) was calculated as follows:

$$CR_{NIR} = \frac{A_{bef}(C_I) + A_{bef}(C_{II})}{A_{bef}(C_I) + A_{bef}(C_{II}) + A_{bef}(Am)} \quad (1)$$

where $A_{bef}(C_I)$ is the integral intensity of the OH band C_I region (6429–6469 cm^{-1}); $A_{bef}(C_{II})$ is the integral intensity of the OH band C_{II} region (6267–6317 cm^{-1}); and $A_{bef}(Am)$ is the integral intensity of the Am region (6949–7532 cm^{-1}).

X-ray diffraction

The D8 Advance X-ray diffractometer (Bruker, Germany) with the two-dimensional (2D) Vantec-500 detector (GADDS-General Detector Diffraction System) and a KFL CU 2K (λ(CuKα) = 1.541840 Å) tube was used for X-ray characterization of natural and deuterated membranes. The diffraction patterns were obtained with 40 kV, 40 mA, with a scanner amplitude of 15.00 (300–900 s) and a collimator of 0.5 mm. Crystallinity index (CR_X) was calculated using (eqn 2) according to the method described by Segal *et al.*[38]

$$CR_X = \frac{I_{200} - I_{amorphous}}{I_{200}} \times 100 \quad (2)$$

I_{200} represents the maximum intensity of the peak 2θ = 22.7°, which corresponds to the (200) plane.

$I_{amorphous}$ represents the lowest intensity between the (200) plane and the (110) peak at 2θ = 14.5, which is the background, and it correlates with the amorphous region of cellulose.[17,38]

Raman spectroscopy

Dried BNC and dBNC films were cut into four parts and mounted, with 3 μl MilliQ drop between each piece. These sandwiches were dried at 60 °C for an additional 3 hours before evaluation. Raman spectroscopy was performed using Witec alpha300RA equipment, which features a solid-state laser at 785 nm to minimize luminescence, a 300 g mm^{-1} grating, and a 40× objective. The chemical mapping was created using 25 × 25 spectra, with an exposure time of 500 ms per spectrum and a power of 25 mW. The data was corrected for cosmic rays and background. The images were produced by integrating the areas under the deuterium-related peaks, representing the intensities of the C–D bond at 2148 cm^{-1} and the O–D bond at 2473 cm^{-1}. Witec Project Five was used to analyze the data and perform the statistical analysis.

SR-μFTIR

One drop of 3 μL of 68 μg mL^{-1} dBNCf was deposited onto a CaF_2 window and dried under vacuum at RT for 16 h. Samples were kept under vacuum until the measurement day to avoid water absorption. A Hyperion 3000 microscope coupled to a Vertex 80 spectrometer (Brucker, Billerica, MA) equipped with a 36× magnification objective was used for Synchrotron Radiation Fourier Transform Infrared microspectroscopy (SR-μFTIR) at the MIRAS beamline at ALBA Synchrotron (Cerdanyola del Vallés, Barcelona, Spain). The spectra were collected in transmission mode using an MCT detector at 4 cm^{-1} spectral resolution, 5 × 5 μm aperture dimensions. A focal plane array (FPA) sensor was used for imaging measurement using the internal source, co-adding 128 scans in the 900–4000 cm^{-1} range. Data was analyzed using OPUS 7.5 (Bruker), Unscrambler X 10.5, and MATLAB R2010b. The color scale ranges from the lowest intensity (blue) to the highest (pink).

Zeta potential

The zeta potential of fibers was analyzed using a Zetasizer ULTRA (Malvern Instruments, UK) after dilution in MilliQ water at a concentration of 68 μg ml^{-1}. Three measurements were performed, and the average Z potential was calculated.

Neutron irradiation

The experiments were carried out at the HISPaNoS facility of the National Accelerator Center (CNA) in Seville.[47] The membranes were evaluated through neutron irradiations using a silicon carbide (SiC) detector fabricated at the National Center for Microelectronics in Barcelona. This device is described in the references.[44,48,49] Two irradiations, each with a duration of 45 minutes, were performed using a continuous fast neutron spectrum (up to 8 MeV), produced by the Be(d,n) nuclear reaction with 4 MeV deuteron beams.[47] The detector was operated at a bias voltage of 200 V, resulting in an active thickness of 20 μm. During the first irradiation, the device was covered with a 50 μm-thick dBNC membrane, as shown in Fig. 5A. In the second irradiation, it was replaced with a non-deuterated membrane of similar characteristics. The detector response was simulated using the PHITS code, based on the Monte Carlo method.[45]

Author contributions

Amanda Muñoz-Juan: writing – original draft, review & editing, validation, methodology, investigation, formal analysis, conceptualization. Daniela Díaz, Judith Marin-Ortega, and Nerea Murugarren: methodology, investigation. Mariano Campoy-Quiles: Raman experiment and analysis, review. Felipe Zamorano, Martín Pérez neutron experiments and formal analysis. Consuelo Guardiola, neutron experiments, formal analysis, and funding acquisition. Anna Laromaine: writing – original draft, review & editing, supervision, resources, funding acquisition, conceptualization, validation.

Conflicts of interest

The authors declare that they have no known competing financial interests or personal relationships that could have influenced the work reported in this paper.

Abbreviations

BNC	Bacterial nanocellulose
dBNC	Deuterated BNC
D-gly	Deuterated glycerol
FT-IR	Fourier transform infrared
SR-μFTIR	Synchrotron radiation-based Fourier transform infrared microspectroscopy
HS	Hestrin-Schramn media
SiC	Silicon carbide
PHITS	Particle and heavy ion transport code system
LET	Linear energy transfer
SEM	Standard error of the mean
CR_X	Cristallinity index from X-ray data
CR_{NIR}	Cristallinity indez from NIR measurements
CNA	Centro nacional de aceleradores
b (unit)	Barn

Data availability

All data supporting the findings of this study is available in the repository digital.csic. https://digital.csic.es/handle/10261/431274 with the DOI: 10.20350/digitalCSIC/18345.

Acknowledgements

SR-μFTIR experiments were performed at the BL01-MIRAS beamline at ALBA Synchrotron with the collaboration of ALBA staff (ID:2020094625). We are grateful to Agustín Mihi (ICMAB-CSIC) for providing access to the NIR spectrometer, supervising the measurements, and guiding in data analysis. This research was supported by the Spanish Ministry of Science and Innovation through the RTI2018-096273-B-I00 and PID2021-122645OB-100 projects, 'Severo Ochoa' Program for Center of Excellence in R&D (CEX2019-000917), the Generalitat de Catalunya (2017SGR765 grant). A. M. J. acknowledges the Ph.D. scholarship (FPU18/05190) in the framework of the Biotechnology Ph.D. program of the UAB. A. M. J. and A. L. participate in the Spanish National Research Council (CSIC) interdisciplinary platform for sustainable plastics towards a circular economy (SusPlast), the Aerogels COST ACTION (CA 18125), the EPNOE network, Conexión Nanomedicina del CSIC, and Red Nanocare 2.0. M. P. thanks funding from the European Union Horizon 2022 research and innovation program under the Marie Sklodowska-Curie grant agreement No. 101106191. C. G. acknowledges the Subvenciones 2022 SUB-08 program from the Spanish Nuclear Safety Council (CSN) and the Spanish government through the 'María de Maeztu Unit of Excellence' accreditation (CEX2023-001397-M). Finally, the authors would like acknowledge the assistance of the ICMAB-CSIC Scientific & Technical Services: X-ray Diffraction Laboratory (Anna Crespi), Spectroscopy Lab and Soft Matter Unit/Unit 6 of the ICTS "NANBIOSIS"; and CNA for their technical support.

References

1 H. Seddiqi, E. Oliaei, H. Honarkar, J. Jin, L. C. Geonzon, R. G. Bacabac and J. Klein-Nulend, *Cellulose*, 2021, **28**, 1893–1931.
2 P. Singh, H. Baniasadi, S. Gupta, R. Ghosh, S. Shaikh, J. Seppälä and A. Kumar, *Int. J. Biol. Macromol.*, 2024, **278**, 134402.
3 S. Yang, Q. Ding, Y. Li and W. Han, *Int. J. Biol. Macromol.*, 2024, **259**, 129203.

4 A. Muñoz-Juan, A. Assié, A. Esteve-Codina, M. Gut, N. Benseny-Cases, B. S. Samuel, E. Dalfó and A. Laromaine, *Carbohydr. Polym.*, 2024, **331**, 121815.
5 Z. Wu, B. Wang, J. Li, R. Wu, M. Jin, H. Zhao, S. Chen and H. Wang, *Nano Lett.*, 2022, **22**, 8152–8160.
6 K. Nyamayaro, P. Keyvani, F. D'Acierno, J. Poisson, Z. M. Hudson, C. A. Michal, J. D. W. Madden, S. G. Hatzikiriakos and P. Mehrkhodavandi, *ACS Appl. Mater. Interfaces*, 2020, **12**, 52182–52191.
7 V. S. Raghuwanshi, Y. Cohen, G. Garnier, C. J. Garvey and G. Garnier, *Macromolecules*, 2021, **54**, 6982–6989.
8 T. Imai, M. Naruse, Y. Horikawa, K. Yaoi, K. Miyazaki and J. Sugiyama, *Cellulose*, 2023, **30**, 8423–8438.
9 J. He, S. V. Pingali, S. P. S. Chundawat, A. Pack, A. D. Jones, P. Langan, B. H. Davison, V. Urban, B. Evans and H. O'Neill, *Cellulose*, 2014, **21**, 927–936.
10 Y. Song, S. Liu, H. Ben, Y. Zhang, G. Han, A. J. Ragauskas and W. Jiang, *Front. Plant Sci.*, 2021, **12**, 709692.
11 J. Su, V. S. Raghuwanshi, W. Raverty, C. J. Garvey, P. J. Holden, M. Gillon, S. A. Holt, R. Tabor, W. Batchelor and G. Garnier, *Sci. Rep.*, 2016, **6**, 36119.
12 Y. Song, X. Meng, W. Jiang, B. R. Evans, H. Ben, Y. Zhang, Y. Pu, S. V. Pingali, B. H. Davison, S. Zhang, G. Han and A. J. Ragauskas, *Cellulose*, 2022, **29**, 4269–4286.
13 S. Cui, Y. Xie, X. Wei, K. Zhang and X. Chen, *Ind. Crops Prod.*, 2022, **187**, 115452.
14 H. O'Neill, R. Shah, B. R. Evans, J. He, S. V. Pingali, S. P. S. Chundawat, A. D. Jones, P. Langan, B. H. Davison and V. Urban, in *Methods in Enzymology*, Academic Press Inc., 2015, vol. 565, pp. 123–146.
15 V. S. Raghuwanshi, J. Su, C. J. Garvey, S. A. Holt, W. Raverty, R. F. Tabor, P. J. Holden, M. Gillon, W. Batchelor and G. Garnier, *Cellulose*, 2017, **24**, 11–20.
16 Y. Song, W. Jiang, H. Ben, Y. Zhang, G. Han and A. J. Ragauskas, *Cellulose*, 2021, **28**, 5351–5361.
17 G. Bali, M. B. Foston, H. M. O'Neill, B. R. Evans, J. He and A. J. Ragauskas, *Carbohydr. Res.*, 2013, **374**, 82–88.
18 A. Uali and A. Aslanbek, *Cellulose*, 2025, **32**, 6463–6475.
19 M. Shao, J. Keum, J. Chen, Y. He, W. Chen, J. F. Browning, J. Jakowski, B. G. Sumpter, I. N. Ivanov, Y. Z. Ma, C. M. Rouleau, S. C. Smith, D. B. Geohegan, K. Hong and K. Xiao, *Nat. Commun.*, 2014, **5**, 4180.
20 L. Li, J. Jakowski, C. Do and K. Hong, *Macromolecules*, 2021, **54**, 3555–3584.
21 M. M. Hosamani, A. Vinayak, G. B. Hiremath, P. N. Patil and N. M. Badiger, *Ann. Nucl. Energy*, 2022, **171**, 109045.
22 A. Radulescu, R. Biehl and A. Papagiannopoulos, *J. Appl. Crystallogr.*, 2025, **58**, 1582–1594.
23 B. An, Y. Deng, Z. Jin and S. Sun, *Adv. Funct. Mater.*, 2025, **35**, 2422522.
24 S. Ghosh, *Comprehensive Materials Processing*, Elsevier, 2nd edn, 2024, vol. 8, pp. 87–98.
25 B. Hamermesh, G. R. Ringo and S. Wexler, *Phys. Rev.*, 1953, **90**, 603–606.
26 L. Kaplan, G. R. Ringo and K. E. Wilzbach, *Phys. Rev.*, 1952, **87**, 785–786.
27 J. Terreni, M. Trottmann, R. Delmelle, A. Heel, P. Trtik, E. H. Lehmann and A. Borgschulte, *J. Phys. Chem. C*, 2018, **122**, 23574–23581.
28 P. Boillat, J. Biesdorf, P. Oberholzer, A. Kaestner and T. J. Schmidt, *J. Electrochem. Soc.*, 2014, **161**, F192–F198.
29 M. Zarebanadkouki, E. Kroener, A. Kaestner and A. Carminati, *Plant Physiol.*, 2014, **166**, 487–499.
30 M. Caresana, M. Ferrarini, G. P. Manessi, M. Silari and V. Varoli, *Nucl. Instrum. Methods Phys. Res., Sect. A*, 2013, **712**, 15–26.
31 R. H. Olsher, H.-H. Hsu, A. Beverding, J. H. Kleck, W. H. Casson, D. G. Vasilik and R. T. Devine, *Health Phys.*, 2000, **79**, 170–181.
32 S. Yue, S. Tabbassum, E. H. Jaye, C. A. M. Anderson and L. H. Nie, *Phys. Eng. Sci. Med.*, 2025, **48**, 35–46.
33 N. Murugarren, S. Roig-Sanchez, I. Antón-Sales, N. Malandain, K. Xu, E. Solano, J. S. Reparaz and A. Laromaine, *Adv. Sci.*, 2022, **9**, 2201947.
34 Y. Li, C. Tian, H. Tian, J. Zhang, X. He, W. Ping and H. Lei, *Appl. Microbiol. Biotechnol.*, 2012, **96**, 1479–1487.
35 S. S. Wang, Y. H. Han, J. L. Chen, D. C. Zhang, X. X. Shi, Y. X. Ye, D. L. Chen and M. Li, *Polymers*, 2018, **10**, 963.
36 C. Recsei, M. Cagnes, R. A. Russell, R. E. Sonstrom and T. Darwish, *Org. Biomol. Chem.*, 2025, **23**, 3380–3392.
37 K. S. Salem, N. K. Kasera, M. A. Rahman, H. Jameel, Y. Habibi, S. J. Eichhorn, A. D. French, L. Pal and L. A. Lucia, *Chem. Soc. Rev.*, 2023, **52**, 6417–6446.
38 L. Segal, J. J. Creely, A. E. Martin and C. M. Conrad, *Text. Res. J.*, 1959, 786–794.
39 T. Inagaki, H. W. Siesler, K. Mitsui and S. Tsuchikawa, *Biomacromolecules*, 2010, **11**, 2300–2305.
40 M. Szymańska-Chargot, J. Cybulska and A. Zdunek, *Sensors*, 2011, **11**, 5543–5560.
41 N. Gierlinger, *Appl. Spectrosc. Rev.*, 2018, **53**, 517–551.
42 H. Satha, I. Kouadri and D. Benachour, *J. Polym. Environ.*, 2020, **28**, 1914–1920.
43 H. Kubota, K. Sakamoto and T. Matsui, *Sci. Rep.*, 2020, **10**, 16426.
44 M. Pérez, F. Zamorano, C. Fleta, B. Fernández, C. Guerrero, P. Godignon, G. Pellegrini, P. Pérez-Maroto and C. Guardiola, *Nucl. Instrum. Methods Phys. Res., Sect. A*, 2024, **1069**, 169968.
45 K. Niita, T. Sato, H. Iwase, H. Nose, H. Nakashima and L. Sihver, *Radiat. Meas.*, 2006, **41**, 1080–1090.
46 J. Singh, T. W. J. Steele and S. Lim, *Biomater. Adv.*, 2023, **144**, 213174.
47 M. A. Millán-Callado, C. Guerrero, B. Fernández, J. Gómez-Camacho, M. Macías and J. M. Quesada, *Radiat. Phys. Chem.*, 2024, **217**, 111464.
48 M. Pérez, F. Zamorano, C. Fleta, C. Muñoz-Montplet, D. Jurado-Bruggeman, M. Jiménez, P. Guardia, G. Grabulosa-Morera, R. Morales-Pérez, G. Rius, P. Godignon, G. Pellegrini and C. Guardiola, *Sci. Rep.*, 2025, **15**, 30543.
49 M. Pérez, J. J. Blostein, F. Zamorano, C. Fleta, J. Marín, G. Pellegrini and C. Guardiola, *Sci. Rep.*, 2026, **16**, 2322.